PHYSICAL REVIEW A VOLUME 44, NUMBER 8 15 OCTOBER 1991

Correlated distributions in g and A tensors at a biologically active low-symmetry cupric site

Alan Aqualino* and Arthur S. Brill
Department of Physics, University of Virginia, Charlottesville, Virginia 22901

Graeme F. Bryce
Roche Dermatologics, Nutley, New Jersey 07110

Bernard S. Gerstman
Department of Physics, Florida International University, Miami, Florida 33199
and Department of Physics, University of Virginia, Charlottesville, Virginia 22901

(Received 18 March 1991)

Frozen-solution EPR spectra from the cupric site in the protein azurin were measured at 6, 9, and 35 GHz, and subjected to a model-independent analysis. Anomalies in the splittings and shapes of the hyperfine peaks of the low-field quartet are faithfully simulated when a correlated distribution in spin-Hamiltonian parameters is employed, with $\Delta A_{11}/\Delta g_{11} = -0.08\ \text{cm}^{-1}$ and $\sigma_g = 0.009$. A hybrid-orbital "united-atom" model is used as the basis for a perturbation calculation of the spin-Hamiltonian parameters. With a simple assumption relating the spreads in the hybridization parameters, these spreads and $\Delta A_{11}/\Delta g_{11}$ are computed from the model. Equipartition is applied to estimate force constants for the protein modes responsible for the distribution in site geometry. With hybridization parameters in ranges constrained to produce agreement between the calculated and observed magnetic-resonance properties, a force constant at the upper end of those for bending modes is obtained for tetrahedral displacement, and a stiffer one, consistent with stretch, is found for displacement around the symmetry axis.

PACS number(s): 87.15.By, 33.35.Ex, 75.10.Dg

INTRODUCTION

Because of the intimate relation between spatial symmetry and orbital angular momentum [1], properties of the spectroscopic (or g) tensor and the hyperfine (or A) tensor can be used to investigate the site symmetry of paramagnetic metal ions. In contrast to the more or less regular symmetries of complexes of metal ions with small ligands, the binding site in a protein is likely to be without any symmetry element. Furthermore, in a protein, the atoms to which the metal ion is bound are part of a macromolecule that, above freezing temperature, is undergoing Brownian conformational dynamics. Many side chains of the protein bear charges which, while having well-defined average values, fluctuate temporally and (because of conformational and charge thermal motion) spatially. Thus a metal ion in a protein is subject to a ligand geometry and an electric field, both of which are of low symmetry and fluctuate. Because of the dependence of the EPR spectrum upon orbital-angular-momentum components, this experimental method is capable of revealing consequences of inhomogeneous, low-symmetry, ligand geometry upon the states of a paramagnetic metal ion. It is not surprising, then, that it is necessary to include distributions in spin-Hamiltonian parameters in the simulation of EPR spectra from cupric and heme sites in proteins [2–5]. The broadness of far-infrared bands of heme-protein complexes has also been attributed to spread in a spin-Hamiltonian parameter [6]. These distributions are associated with the ensemble of protein conformations frozen in as the temperature is lowered to the cryogenic region of the measurements [7,8]. In the case of aquoferric myoglobin, the distributions in electronic-energy-level differences from which the distributions in spin-Hamiltonian parameters arise have been quantified, both in solution and in the crystalline state [9]. In this paper we report the microwave frequency dependence of EPR spectra from the cupric protein azurin, in frozen solution at cryogenic temperatures, measurements which demonstrate and quantify a correlation between the distributions in two spin-Hamiltonian parameters.

Azurin is ideal for studying the chemical and physical structure of blue copper proteins because it contains only one copper, has a low molecular weight (14 000), and is obtainable from many bacterial sources. Thus there is a substantial literature on azurin, including reports of three-dimensional structure from x-ray diffraction [10,11], optical absorptivity [3,12], circular dichroism [3,13, 14], and magnetic circular dichroism [14, 15]. The atoms closest to the copper are two imidazole nitrogens and a thiolate sulfur at 2.0–2.2 Å, and there is a thioether sulfur at about 2.8 Å [11]. Because of delocalization of electron (hole) spin onto the near atoms, hyperfine interaction with the nitrogen nuclei (spin 1) is expected. Such has been observed by electron-nuclear double resonance (ENDOR) spectroscopy on a blue copper protein related to azurin, stellacyanin, where splittings of about $0.0014\ \text{cm}^{-1}$ are found [16]. Ligand hyperfine splittings of this magnitude are not resolved in the broad resonances of the EPR spectra from these cupric sites; rather they are one of the sources contributing to the width of the envelope of each band of the copper hyperfine quartet.

The hybrid-atomic-orbital model (HAOM) of low-symmetry cupric sites, originally used by Bates *et al.* [17], employs only about ten orbital parameters to account for magnetic, optical, and magneto-optical properties [2,18,19]. The most recent application of the HAOM was to the linear-electric-field effect [20]. In the HAOM, molecular orbitals are approximated by orbitals of a united atom; angular dependence is expressed in the same way as for atomic orbitals, but the radial functions are expanded. Because the cupric hole is fractionally delocalized onto ligand atoms, spin-orbit coupling constants are, in effect, reduced from their free-ion values. The orbital reduction factor, often used to account for this effect, is replaced in the HAOM treatment below by radial delocalization factors appropriate to specific orbitals [3]. Taken together, the parameters of the HAOM provide a relatively simple description of the angular dependence and delocalization of hole density in the ground and low-lying excited states. Distributions in certain of these parameters further provide an explanation of the results of the experiments reported in this paper, and a practical means of describing at least some of the effects of conformational and charge inhomogeneity upon atoms in a macromolecule.

The microwave frequency dependence of EPR hyperfine linewidths in square-planar cupric complexes with relatively small ligands in frozen solution has been investigated [21]. Alternative formulations of the results were presented, one a phenomenological description, the other based upon molecular in-plane σ- and π-bonding parameters, and both depending upon a correlation in distributions. In azurin EPR spectra, because the hyperfine peaks overlap strongly, it is not possible to measure the linewidths, and simulations rather than analytical expressions are necessary for obtaining the parameters which characterize the cupric site.

EXPERIMENT

Varian V-4500 and V-4561 microwave bridges were used to obtain azurin EPR spectra at 9 and 35 GHz, respectively. For EPR spectroscopy at 9 GHz, a quartz-Pyrex X-band Dewar was used to keep the sample at 77 K, while a Varian V-4547 variable temperature Dewar was employed to achieve temperatures above 77 K. The *Ka*-band (35 GHz) Dewar was modeled from a design by Professor J. J. Villafranca, Pennsylvania State University, wherein cold gas cools the Varian V-4566 cavity, with a lower limit of 110 K at the sample. Analysis of *X*- and *Ka*-band spectra measured with the above apparatus suggested that close to optimum resolution of the quartet bands would be achieved at 6 GHz. A 6-GHz bridge based upon a reflection cavity operating in the TE_{102} mode was, therefore, designed and built, with features similar to those of higher microwave frequency EPR apparatus. In all experiments reported here, the microwave power incident upon the same was less than 50 mW, although no saturation effects were apparent even at 200 mW.

Azurin was isolated from *Pseudomonas aeruginosa* and purified as described earlier [12]. Low molecular-weight contaminants (e.g., ferricyanide used in a previous step to insure maximal conversion to the cupric form) were removed by passing a freshly centrifuged solution through G-25 Sephadex. The protein was then concentrated by dialysis against saturated ammonium sulfate, and returned to low ionic strength by dialysis against 10 m*M* phosphate buffer, *p*H 7. The final concentration of azurin solutions for EPR measurements was about 6 m*M*, with spectrophotometric purity values (ratio of peak absorbance at 625 nm to that at 280 nm) in the range 0.56–0.58.

RESULTS

J-band spectrum. The EPR spectrum at 6.077 GHz appears axial, Fig. 1. Copper (nuclear spin $\frac{3}{2}$) hyperfine structure is observed in the low-field (g_{11}) region, but not in the high-field (g_{22},g_{33}) region. We define ΔB_{ij} as the hyperfine interval between peaks i and j, with i at lower field than j. The 50-G hyperfine interval ΔB_{12} between

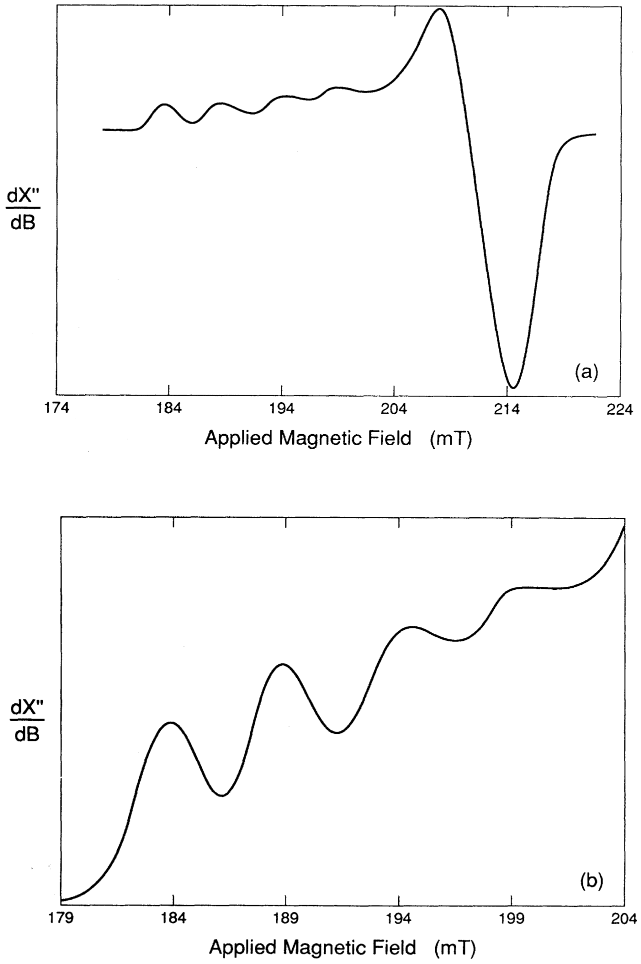

FIG. 1. Azurin EPR spectrum observed at 6.077 GHz, 77 K. The expanded low-field region shown in (b) was taken at greater gain than the record of (a).

peaks 1 and 2 (the two lowest-field peaks) is clearly smaller than ΔB_{23}, about 57 G. ΔB_{34} is approximately 55 G. Because simulations based upon normal first- and second-order hyperfine effects cannot produce this asymmetry, it is impossible to assign accurate spin-Hamiltonian parameters without a quantitative explanation of the phenomenon. The g value corresponding to the central trough of the J-band low-field quartet is 2.270.

X-band spectrum. The low-field region is more poorly resolved at 9.240 GHz, Fig. 2, than at the J-band frequency. Because the magnetic-field separation between the g_{11} and g_{22},g_{33} regions increases as the microwave frequency increases, the poorer resolution of peak 4 is surprising. In general, the bands of the low-field quartet in Fig. 2 are somewhat less revolved than in an earlier published X-band spectrum [12], and more like those in a recent report from another laboratory [22]. (See Discussion.) ΔB_{34} is noticeably smaller than $\Delta B_{12}=54$ G and $\Delta B_{23}=58$ G. The g value associated with the location of the trough between peaks 2 and 3 is 2.266.

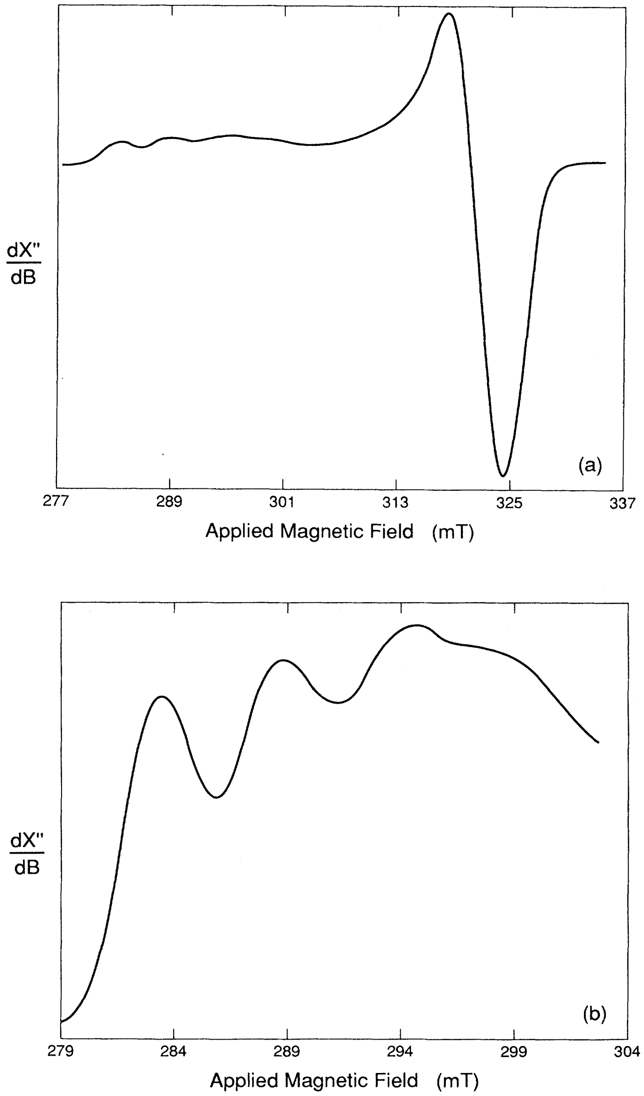

FIG. 2. Azurin EPR spectrum observed at 9.240 GHz, 77 K. The expanded low-field region shown in (b) was taken at greater gain than the record of (a).

Ka-band spectrum. At 35.2 GHz, there is little interference between the g_{11} and g_{22},g_{33} regions of the EPR spectrum, Fig. 3. The shape of the high-field region at this frequency agrees with other measurements [22, 23] and with the predicted rhombic character of the cupric site in azurin [18]. Simulated 35-GHz frozen-solution spectra [24] of this high-field region match experiment when $g_{22}=2.053\pm0.001$ and $g_{33}=2.036\pm0.001$. Unresolved hyperfine splittings contribute to line broadening in the high-field region. When unrealistically narrow (10 G) peak-to-trough widths are used for the Gaussian lines

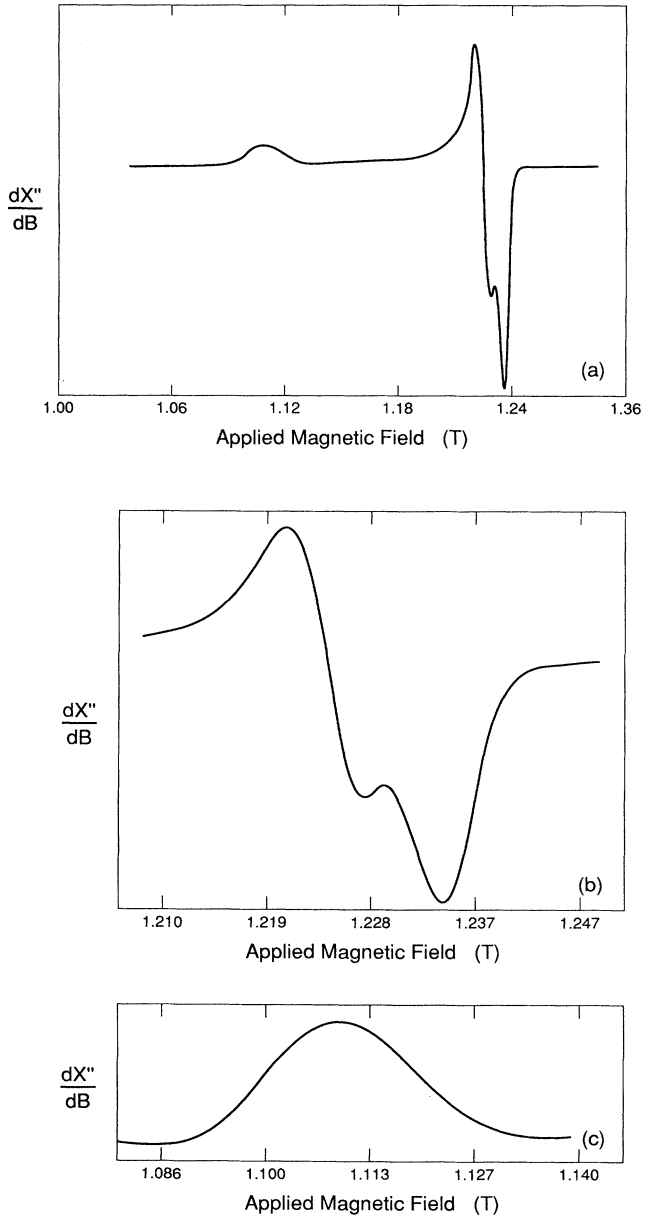

FIG. 3. Azurin EPR spectrum observed at 35.2 GHz, 110 K. The expanded low-field region shown in (c) was taken at greater gain than the records of (a) and (b).

in simulations, the splitting required to match the broad experimental resonance sets an upper limit on the magnitudes of A_{22} and A_{33} (taken equal) of 0.0018 cm^{-1}. When the linewidth is set at 16 G rms, found to be effective in simulating the onset of lowest-field absorption, a realistic match to the high-field region is achieved with $|A_{22}|=0.0015\pm0.0002$ and $|A_{33}|=0.0016\pm0.0002$ cm^{-1}. The low-field hyperfine quartet observed at *J*- and *X*-band frequencies is collapsed at the *Ka*-band frequency into a single, broad peak, centered at $g=2.269$ and slightly sharper on its downfield edge. This absence of resolved splittings, expected to be of the order of 50–55 G, is not predicted by normal frozen-solution simulations, and complicates determination of spin-Hamiltonian parameters.

ANALYSIS OF FREQUENCY-DEPENDENT SPECTRA

Several possibilities have been considered for the origin of the unequal separations between hyperfine peaks and for the microwave frequency dependence of these separations. Due to the difference in magnetogyric ratio of the two major copper isotopes, the hyperfine splitting from ^{65}Cu is slightly larger than from ^{63}Cu. This isotopic difference in nuclear moment would manifest itself as resolved structure at $m_i=\pm\frac{3}{2}$ if the linewidth were very narrow (i.e., six hyperfine lines rather than four). However, computer simulations for realistic linewidths show four equally separated, broadened, but well-resolved hyperfine peaks. The isotopic difference in nuclear magnetic moment cannot be the cause of the observed unequal hyperfine splittings.

Second-order treatment of the spin-Hamiltonian perturbation in the general case, with noncoinciding principal axes of the g and A tensors, shows small changes in hyperfine separation which are expected [25] and have been measured [26] to vary monotonically across the hyperfine manifold. The magnitude of the changes is also expected to be inversely proportional to the microwave frequency. These properties cannot explain the behavior of the low-field quartet from azurin. Simulations have shown that even an extreme noncoincidence of the principal z directions for the g and A tensors does not result in collapse of hyperfine structure at 35 GHz.

X-band EPR spectra of cupric acetate in 60% glycerol, 40% water at 243 K show an increase in the width of the hyperfine peaks at higher field [27]. Because a negative correlation between g and $|A|$ would associate increased hyperfine splittings with decreased g values [28], this field-dependent broadening was hypothesized to be a consequence of such a correlated statistical variation in the spin-Hamiltonian parameters [27]. Figure 4 demonstrates how negative correlation in a two component model broadens the upfield hyperfine peaks while leaving the downfield peak approximately stationary. Since the g variations arising from sample inhomogeneties probably result in microwave frequency-dependent hyperfine linewidths, it was suggested by Hill [23] that such statistical variations might be the basis for the anomalous low-field EPR behavior of azurin. The statistical contributions of various (g,A) pairings are likely to be well described by a bivariate Gaussian distribution centered about mean values g_0, A_0. If the respective standard deviations are labeled σ_g and σ_A, then [29]

$$P(A,g)=\frac{1}{2\pi\sigma_g\sigma_A(1-\rho^2)^{1/2}}\exp\left\{-\frac{1}{2(1-\rho^2)}\left[\left[\frac{g-g_0}{\sigma_g}\right]^2+\left[\frac{A-A_0}{\sigma_A}\right]^2-2\rho(g-g_0)\frac{A-A_0}{\sigma_g\sigma_A}\right]\right\}, \tag{1}$$

where ρ is the correlation coefficient, defined by

$$\rho\equiv\frac{\mathrm{covar}(g,A)}{\sqrt{\mathrm{var}(A)\mathrm{var}(g)}}=\frac{\langle Ag\rangle-A_0g_0}{\sigma_g\sigma_A}\ .$$

Ideally, simulation of azurinlike EPR spectra would be investigated by summing members of a library of spectra generated from random combinations of g_{11} and A_{11} with weights given by Eq. (1) for various values of ρ, g_0, A_0, σ_g, and σ_A. Some constraint of this elegant procedure is necessitated by the extent of computer resources required to do the calculation, and a particular simplification, used below, is justified by other observations.

Figure 9-5 of Ref. [30], which is a plot of the mean values of $|A_{11}|$ vs g_{11} for several classes of cupric complex, shows that there is a nearly perfect negative correlation between these parameters from cupric sites in proteins ("type 1") closely related to the azurin studied here. Library spectra therefore were generated with the assumption of the linear relation

$$A=A_0+S(g-g_0)\ , \tag{2}$$

where the mean value of g_0 was taken to be 2.269 and that of A_0 either 0.005 25 or 0.0056 cm^{-1}. Gaussian lines of rms width 16 G were used. Eighty such library spectra, from $g=2.230$ to 2.309 in increments of

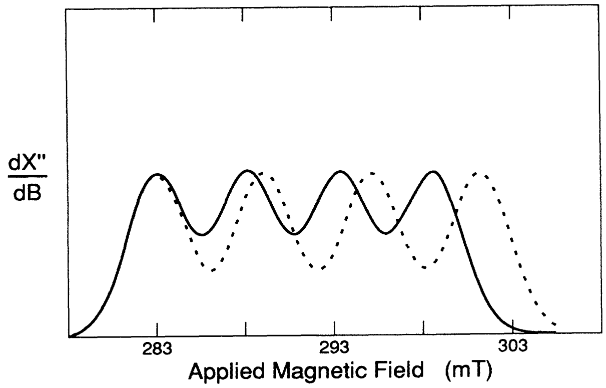

FIG. 4. Two (*X*-band) single-site simulations correlated by $dA/dg=-0.09\ \mathrm{cm}^{-1}$.

$\Delta g = 0.001$, then were summed on the basis of a univariate Gaussian distribution in g. These "distributed" simulations of the 35-GHz low-field region reproduced the basic shape observed experimentally even for $|S| = 0.01$ cm^{-1}, although both the sharpness of the downfield edge and g corresponding to the center of the broad resonance increased slightly with $|S|$. The ability of the distribution hypothesis to account for the observed spectral properties was tested by simulations at lower frequencies. Spectra were simulated at both 6.077 and 9.240 GHz. Characteristic features of the low-field spectra were

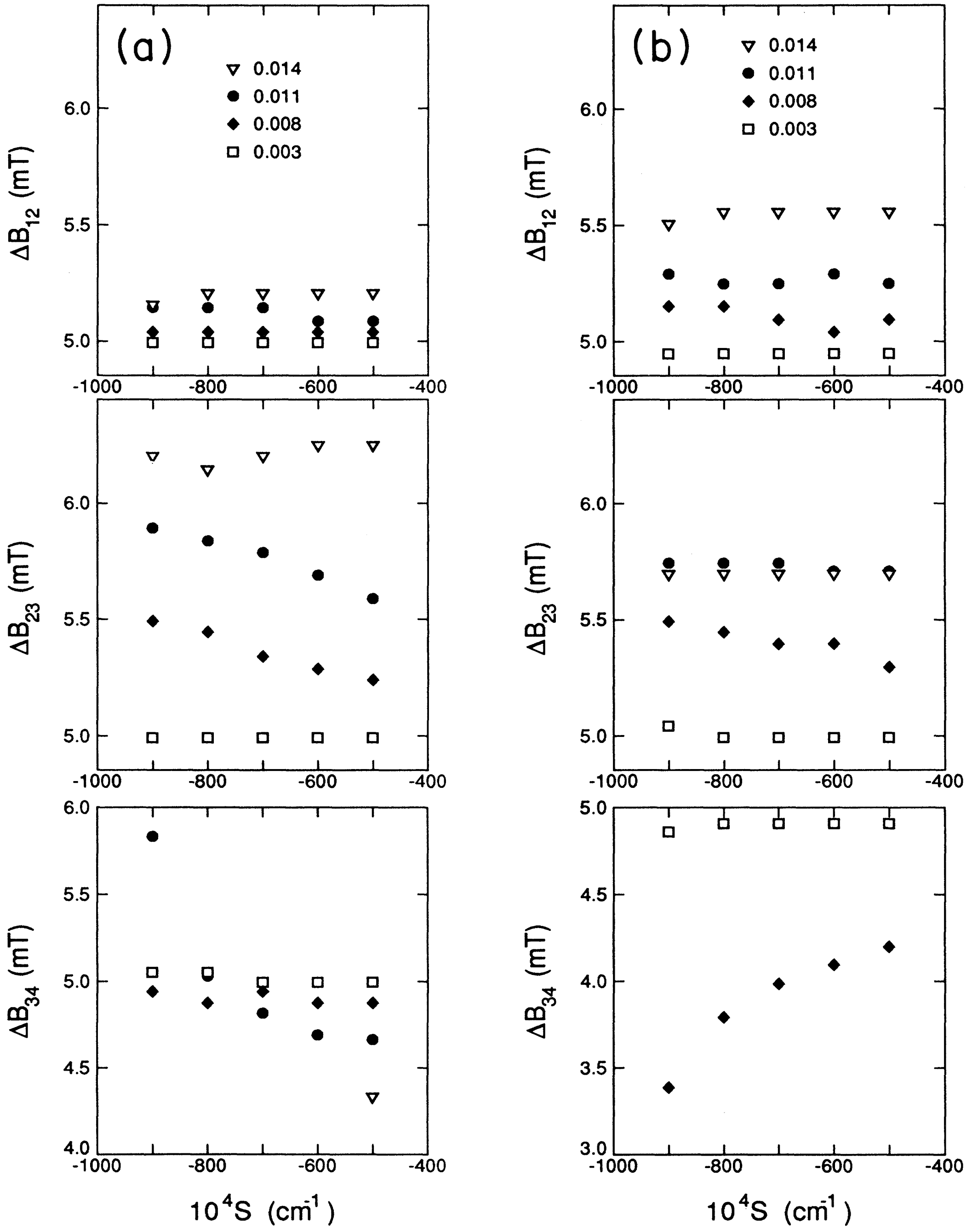

FIG. 5. For the simulations upon which Figs. 5–9 are based, a set of 80 library spectra were generated for each of five different correlation parameters S (the horizontal axis in each plot). The 80 spectra in each set's resultant spectrum were measured and plotted for four standard deviation values (σ_g): □,0.003; ◆,0.008; ●,0.011; ▽,0.014. Less than four data points at any value of S used in the simulation indicates the feature plotted was not resolved at all four standard deviations. ΔB_{12} is the magnetic-field separation (±0.05 mT) between the two lowest-field hyperfine peaks, ΔB_{23} is the analogous separation between peaks 2 and 3, and ΔB_{34} is the spread between the two highest low-field peaks. (a) data are for 6.077 GHz, while the (b) data are for 9.240 GHz, both with a mean A value taken to be $A_0 = 52.5 \times 10^{-4}$ cm^{-1}.

determined for several standard deviations in g (namely, $\sigma_g=0.003$, 0.008, 0.011, and 0.014) and plotted as a function of the correlation parameter S of Eq. (2). Simulations with $\sigma_g=0.003$ closely approximate the case of single g and A tensors since the effects of a distribution are not discernable for smaller standard deviations in g.

Figures 5–8 show representative plots of the information obtained from simulations of EPR spectra based upon the distributions just described. In the J-band simulations, the magnetic-field separation between peaks 1 and 2, ΔB_{12}, is affected little by σ_g and not at all by S. No simulated ΔB_{12} is less than the mean A value used to generate the spectra [e.g., 0.00 525 cm^{-1} or 4.95 mT for Fig. 5(a)], regardless of other distribution parameters. In the 6.077-GHz simulations for $\sigma_g>0.003, \Delta B_{12}$ is always smaller than ΔB_{23}, in accord with experiment. The separations between successive hyperfine peaks in X-band simulations resemble those in the experimental X-band spectrum; i.e., ΔB_{23} is the largest separation and ΔB_{34} is the smallest. Note that, at X band, ΔB_{34} decreases with increasing $|S|$ such that peak 4 can become unresolved when the values assigned to S and σ_g permit this. The ΔB_{23} intervals from the simulations at 6.077 and 9.240 GHz are consistent with the experimental data taken at these two frequencies when $\sigma_g<0.014$.

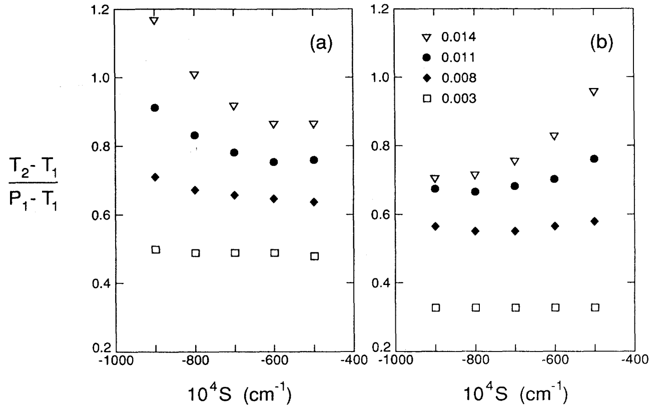

FIG. 7. The ordinate is the difference in height between the first and second troughs (T_2-T_1) in units of the difference in height between the first peak and the first trough, where the troughs are numbered consecutively starting with the one slightly upfield from the first (lowest-field) peak. The plots shown are for $A=52.5\times10^{-4}$ cm^{-1}. The microwave frequencies (in GHz) are (a) 6.077 and (b) 9.240.

In a similar manner, plots (some are shown in Figs. 6–8) of simulated low-field trough separations, g values calculated from the central troughs, and shape and width factors, are used to constrain the parameters to ranges for which simulations of J- and X-band spectra, Fig. 9, are in agreement with their experimental counterparts. This agreement is remarkably good in view of the approximations. Because the actual absorption bands are not purely Gaussian, and nitrogen hyperfine structure from the two imidazole ligands [10,11] has not been explicitly included, it is unlikely that simulations based upon Gaussian line shapes can reproduce the observed spectra entirely faithfully. Furthermore, while the g values may be distributed approximately according to a Gaussian, the actual distribution need not be exactly symmetric or even continuous. The parameters that produce agreement with the EPR spectra at all three microwave frequencies are.

$$\langle g_{11}\rangle=g_0=2.269,\quad g_{22}=2.053,\quad g_{33}=2.036\ ,$$

$$\langle|A_{11}|\rangle=A_0=0.0054\ \text{cm}^{-}1,\quad |A_{22}|=0.0015\ \text{cm}^{-1}\ ,$$

$$|A_{33}|=0.0016\ \text{cm}^{-1}\ ,$$

$$S=-0.08\ \text{cm}^{-1},\quad \sigma_g=0.009\ .$$

DEPENDENCE OF LINEWIDTHS UPON m_I AND FREQUENCY

The parameters plotted in Figs. 7 and 8 show that peak 1 is better resolved at the J-band frequency when $|S|\simeq0.06$ cm^{-1}, and better resolved at the X-band fre-

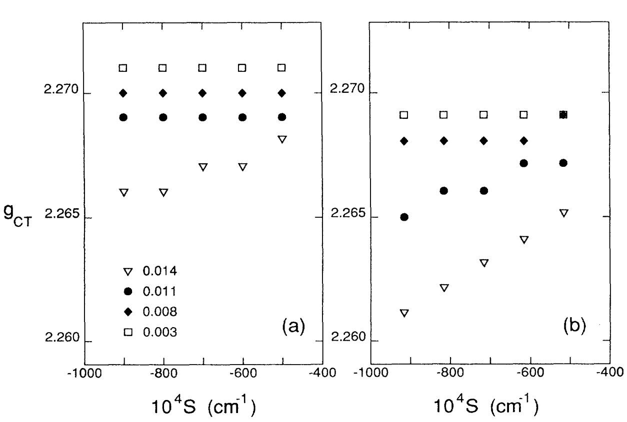

FIG. 6. g_{CT} is the g value associated with the low-field central trough. The plotted data are from simulations in which $A_0=52.5\times10^{-4}$ cm^{-1}. The microwave frequencies (in GHz) are (a) 6.077 and (b) 9.240.

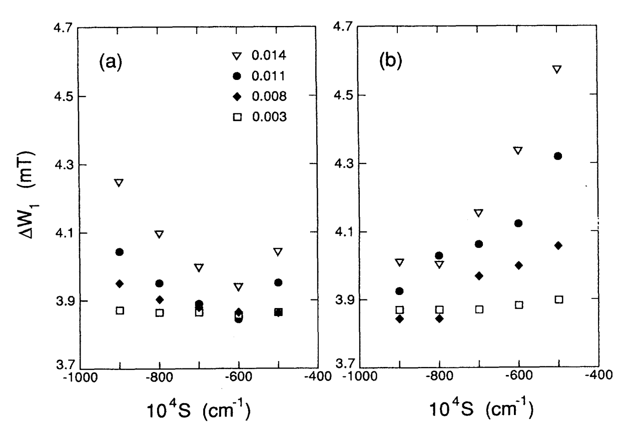

FIG. 8. The ordinate is the full width at half maximum (in mT) for the peak at lowest field. The plots shown are for $A_0=52.5\times10^{-4}$ cm^{-1}. The microwave frequencies (in GHz) are (a) 6.077 and (b) 9.240.

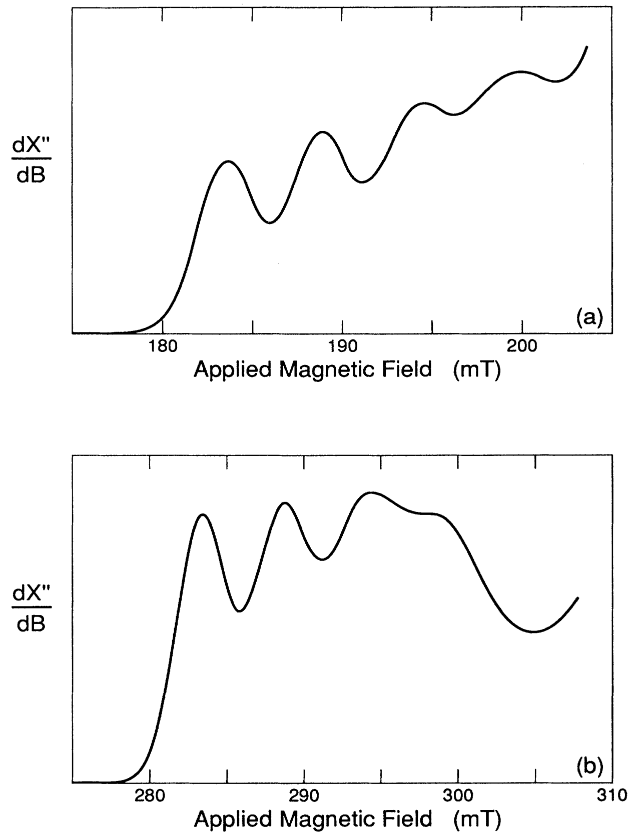

FIG. 9. Sample frozen-solution EPR spectra simulated with a distributed site model: $g_0=2.269, A_0=54\times10^{-4}$ cm^{-1}, $dA/dg=-0.08$ cm^{-1},$\sigma_g=0.009$. The J-band spectrum in (a) should be compared with the experimental spectrum, Fig. 1; the X-band spectrum in (b), with Fig. 2.

quency when $|S|\simeq0.09$ cm^{-1}. For these correlation factors at the respective microwave frequencies, peak 1 remains stationary, e.g., a shift upfield due to a decrease in g is offset by the downfield shift concomitant with an increase in $|A|$. A quantitative basis for this phenomenon was formulated by Froncisz and Hyde in considering the dependence of linewidths upon m_I as observed in square-planar complexes of relatively small ligands with the cupric ion [21]. For a cupric complex with a low-field EPR spectrum characterized by g_0 and A_0, the resonance field corresponding to the level m_I is

$$B_m=(h\nu-m_I A_0)/g_0\mu_B \ .$$

Small changes Δg and ΔA shift this field by

$$\Delta B_m=(m_I A_0-h\nu)(\Delta g/g_0^2\mu_B)-m_I(\Delta A/g_0\mu_B) \ . \quad (3)$$

Equation (3) predicts that the resonance field will not shift if the changes in Δg and ΔA are correlated such that, with $S=\Delta A/\Delta g$,

$$S=A_0/g_0-h\nu/g_0 m_I \ . \quad (4)$$

Because $h\nu/A_0$ is in the range 40–240 for azurin ($A_0\simeq0.005$ cm^{-1}) when the microwave frequency is between 6 and 36 GHz, the first term of Eq. (4) has little influence. Peak 1 ($m_I=\frac{3}{2}$ if $A>0$) therefore should be stationary at 6.1 GHz if $S=-0.06$ cm^{-1}, and at 9.2 GHz if $S=-0.09$ cm^{-1}. These predictions agree well with the behavior noted in Figs. 7 and 8.

While the *extrema* in a frozen solution, first derivative, EPR spectrum are proportional to the actual absorption lines observed in a single crystal [31], the locations and shapes of the low-field $m_I=\frac{1}{2}$ hyperfine peaks reported here at J-, X-, and Ka-band frequencies could be influenced by the effects of averaging over orientations associated with frozen solution spectra as well as by the effects described by Eq. (3). In any case, from Eq. (3), the values of S at which peak 2 is stationary in the absorption spectrum are -0.018 cm^{-1} at the J-band and -0.27 cm^{-1} at the X-band frequencies. Within the range of S used in the simulations under discussion here, the separation between peaks 1 and 2 should be more affected at the X-band frequency than at the J-band frequency by a distribution, a feature shown by Fig. 5.

The linearity of Eq. (3) requires that a symmetric distribution of spin-Hamiltonian parameters not shift the hyperfine band centers in a single crystal. However, a Gaussian distribution in spin-Hamiltonian parameters can broaden a Gaussian-shaped hyperfine peak from an *rms* linewidth of w_0 in the absence of distribution to

$$w=(w_0^2+\overline{\Delta B_m^2})^{1/2} \ , \quad (5)$$

where $\overline{\Delta B_m^2}$ is the variance of the distribution in B_m [21]. The latter variance can be written, with Eq. (3), as

$$\overline{\Delta B_m^2}=(h\nu/g_0^2\mu_B)^2\sigma_g^2+2m_I(h\nu/g_0^3\mu_B^2)(\sigma_{gA}^2-A_0\sigma_g^2/g_0)$$
$$+(m_I^2/g_0^2\mu_B^{2)}(\sigma_A^2+A_0^2\sigma_g^2/g_0^2-2A_0\sigma_{gA}^2/g_0) \quad (6)$$

where $\sigma_g^2\equiv\overline{\Delta g\Delta g}$, $\sigma_A^2\equiv\overline{\Delta A\Delta A}$, and the covariance $\sigma_{gA}^2\equiv\overline{\Delta g\Delta A}$ is nonzero when g and A are correlated. Linewidth differences within the hyperfine quartet are associated with the m_I terms. Because $A_0\ll h\nu$, noticeable linewidth differences between resolved $\pm m_I$ absorption peaks require significant covariance. Even if Eq. (6) quantitatively described the behavior of all four low-field hyperfine peaks in frozen solution, first derivative spectra from azurin, the poor resolution of the experimental peaks precludes direct determination of distribution parameters via comparison between the formulation above and experiment. For example, the best resolved hyperfine peak in the X- and J-band spectra (the one lowest field) is not adequate enough to test the frequency dependence of Eq. (6) because the predicted difference (0.3 G) is less than the experimental accuracy (±0.5 G). Although Eq. (6) may not be useful in quantifying the behavior of the individual hyperfine peaks from azurin, and simulations are therefore essential, the equation does provide insight into the m_I and frequency dependences of spectral features.

With $\sigma_A=S\sigma_g$ and $\sigma_{gA}=S\sigma_g^2$, and the values of $g_0,\sigma_g, A_0,S,$ and w_0 obtained from simulating the experi-

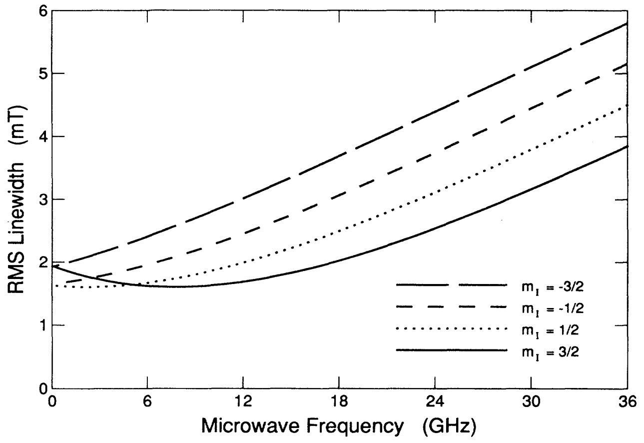

FIG. 10. Dependence upon microwave frequency of rms linewidths of hyperfine peaks in the low-field region. Parameters are those of Fig. 9.

mental spectra, single-crystal linewidths can be calculated from Eq. (5). As shown in Fig. 10, the contribution from the first term of Eq. (6) dominates all four linewidths at microwave frequencies above 20 GHz. The minimum widths of the first and second peaks are at 8.2 and 2.7 GHz, respectively. The apparent narrowing of the upfield peaks at very low frequency does not improve their resolution because of the concomitant confluence of the resonance fields associated with g_{11} and g_{22} , g_{33}. Low microwave frequencies can be useful for complexes with $|S|$ smaller than in azurin because the frequency at which the linewidths are minimized increases with $|S|$, Fig. 11.

Equation (5) was used to plot the azurin EPR absorption that would result if a single crystal, with the same spin-Hamiltonian properties as above, were oriented such that the external magnetic field was along the principal g_{11} direction, Figs. 12–14. At *J*- and *Ka*-band frequencies there would be some improvement in the resolution

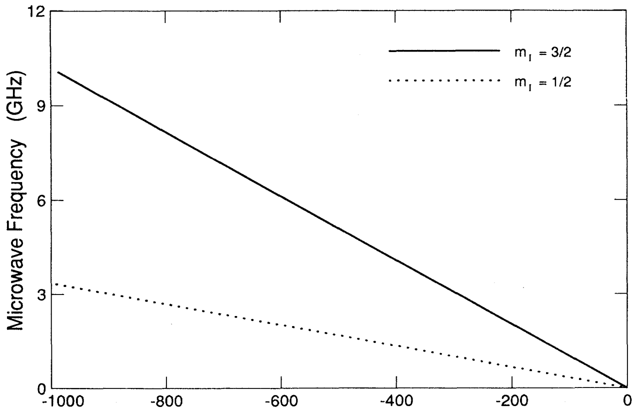

FIG. 11. Microwave frequency at which linewidths of the two lowest-field hyperfine peaks are minimized, as a function of *S*.

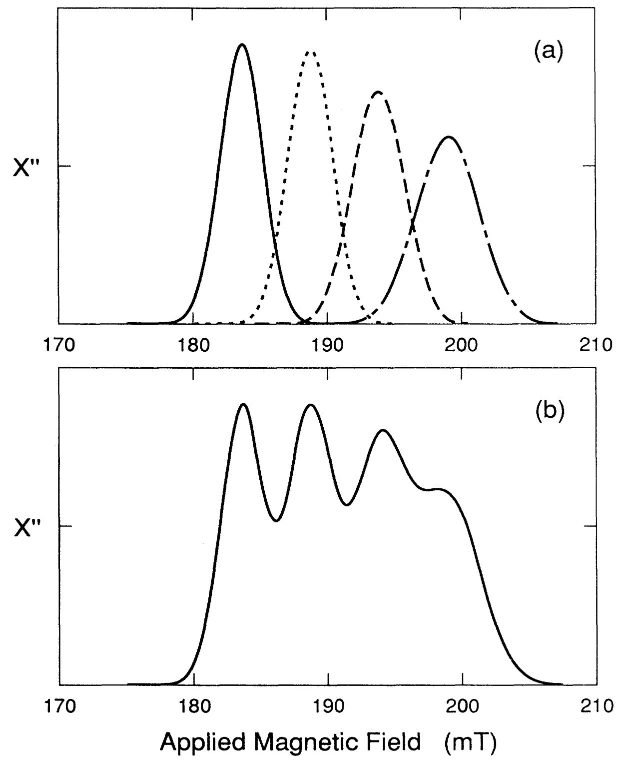

FIG. 12. EPR absorption predicted from single-crystal of azurin at 6.077 GHz. Parameters are those of Fig. 9. (a) shows the members of the quartet separately and (b) shows their envelope.

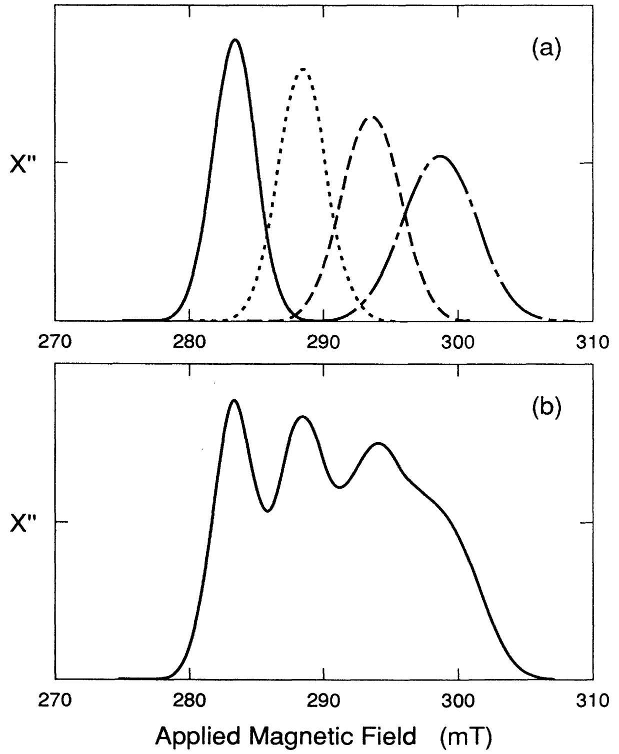

FIG. 13. As in Fig. 12, but for a microwave frequency of 9.240 GHz.

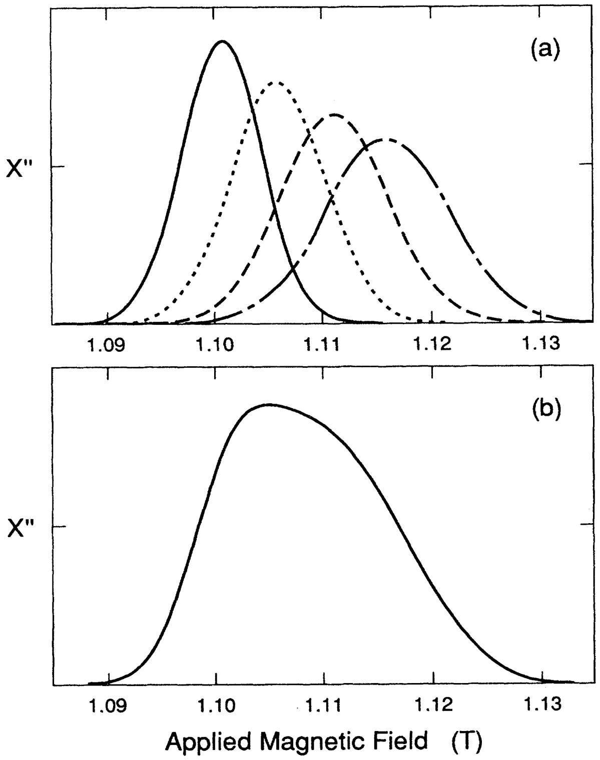

FIG. 14. As in Fig. 12, but for a microwave frequency of 35.2 GHz.

and regularity of the low-field quartet, but the location of the fourth peak would remain poorly defined.

HYBRID-ATOMIC-ORBITAL MODEL OF CUPRIC HOLE STATES

The cupric hole is associated with the metal and all surrounding atoms. (In azurin, these are the two nitrogens and two sulfurs described in the Introduction.) States of such a system are often approximated by mixing metal orbitals with ligand functions constructed as linear combinations of orbitals on the neighboring atoms. In a distinctly different description, nuclei of the atoms involved in the metal site are viewed as coalescing to form, together with surrounding electrons in an appropriate configuration, a single united atom. In this approach, the ligand orbitals become united-atom orbitals of the same symmetry as metal ion orbitals.

All of the optical, magnetic, and magneto-optical properties of the metal site in cupric blue proteins like azurin are consistent with low symmetry [18–20, 32]. While the cupric site is almost certainly without any element of symmetry, models with the low symmetry of point group D_2 have been found to provide a good starting point for calculating spectral and magnetic properties, with deviations from D_2 added when necessary [2,18–20]. At the start, the states are expressed as linear combinations of atomic orbitals belonging to irreducible representations of D_2, a hybrid-atomic-orbital model (HAOM) with which orbital-angular-momentum calculations can readily be made. All of the states shown in Table I belong to irreducible representations of D_2 except the ground state, into which a small amount of 4s is introduced to account, in part, for the unusually small hyperfine splitting $|A_{\parallel}|$ in azurin [2]. Alternative ordering (by energy) of the excited states is considered below.

In order to calculate quantitatively the principal values of the g and A tensors, it is necessary to include the effects of delocalization of the cupric hole onto ligand atoms. In the HAOM, this can be done with radial delocalization factors [3], f_i, which are related to orbital reduction factors [33]; the latter are the fraction of free-ion spin-orbit coupling remaining after complex formation, and are closely approximated by f_i^2. For example, the radial dependence of the $|4p_y\rangle$ united-atom orbital can be expressed in terms of the copper radial function $R_{4p}(r)$ and an expanded radial function $R_{\text{exp}}(r)$ associated with the ligand contribution:

$$|4p_y\rangle = |p_y\rangle[f_y|R_{4p}\rangle + (1-f_y^2)^{1/2} R_{\text{exp}}\rangle] ,$$

where $1-f_y^2$ is that fraction of the hole which is too delocalized to resemble a cupric 4p orbital. For operators which depend inversely upon the cube (or higher power) of the radius, like spin-orbit coupling, matrix elements will be reduced from the free cupric ion value; e.g.,

TABLE I. Hybrid-atomic-orbital model energy-level diagram for the single cupric hole in azurin.

$$|B_3'\rangle = (1-\beta_3^2)^{1/2}|3d_{yz}\rangle - \beta_3|4p_x\rangle$$

$$|B_2'\rangle = (1-\beta_2^2)^{1/2}|3d_{xz}\rangle - \beta_2|4p_y\rangle$$

$$|B_1'\rangle = \frac{1}{[1+\rho^2(1+\sigma^2)]^{1/2}}[\rho(1+\sigma^2)^{1/2}|3d_{xy}\rangle - 4p_z\rangle]$$

$$|B_3\rangle = \beta_3|3d_{yz}\rangle + (1-\beta_2^2)^{1/2}|4p_x\rangle$$

$$|B_2\rangle = \beta_2|3d_{xz}\rangle + (1-\beta_2^2)^{1/2}|4p_y\rangle$$

$$|A_1'\rangle = \frac{1}{[(1+\delta^2)(1+\gamma)^2]^{1/2}}[|3d_{x^2-y^2}\rangle - \delta(1+\gamma^2)^{1/2}|3d_z^2\rangle + \gamma|4s\rangle]$$

$$|A_1\rangle = \frac{1}{[(1+\delta^2)(1+\gamma)^2]^{1/2}}[\delta|3d_{x^2-y^2}\rangle + (1+\gamma^2)^{1/2}|3d_z^2\rangle + \gamma\delta|4s\rangle]$$

$$|B_1\rangle_{\text{mod}} = \frac{1}{[(1+\rho^2)(1+\sigma^2)+(\gamma\sigma)^2]^{1/2}}[|3d_{xy}\rangle + \rho(1+\sigma^2)^{1/2}|4p_z\rangle + \sigma|4s\rangle - \gamma\sigma|3d_{x^2-y^2}\rangle]$$

$$\begin{aligned}\langle 4p_y|\lambda(r^{-3})|4p_y\rangle &= f_y^2\langle\lambda(r^{-3})\rangle_{\text{copper}4p}\\ &\quad +(1-f_y^2)\langle\lambda(r^{-3})\rangle_{\text{exp}}\\ &\simeq f_y^2\lambda_{\text{free ion}}\end{aligned}$$

where the contributions from overlap and $\langle\lambda(r^{-3})\rangle_{\text{exp}}$ are small (but not negligible, as can be seen when the bound cysteine sulfur, with $\lambda=-382\ \text{cm}^{-1}$, is explicitly included [34].) Conversely, electric dipole matrix elements, which are proportional to $\langle r\rangle$, can be greater when delocalization is present than for the free cupric ion. Delocalization from $|3d_{xy}\rangle$, $|3d_{xz}\rangle$, and $|3d_{yz}\rangle$ is not included explicitly. (The admixtures of $|4p_i\rangle$—and of $|4s\rangle$ in $|B_1\rangle$—already reflect bond formation with ligand atoms.) Delocalization is taken to be the same in states $|A_1\rangle$ and $|A_1'\rangle$, and is quantified by the radial delocalization factor f_{A1}.

The principal g and A values have been formulated by two standard methods [17,35] with the following results:

$$\begin{aligned}g_{11}-2.0023 &= \{-8\lambda/[(1+\rho^2)(1+\sigma^2)+(\gamma\sigma)^2]\}\{[f_{A1}/(1+\delta^2)(1+\gamma^2)](\delta^2/E_{A1}+1/E'_{A1})\\ &\qquad +(\gamma\sigma\rho)^2(1+\sigma^2)/[1+\rho^2(1+\sigma^2)]E'_{B1}\}\ , \end{aligned} \tag{7}$$

$$\begin{aligned}g_{22}-2.0023 &= -\{2/[(1+\rho^2)(1+\sigma^2)+(\gamma\sigma)^2]\}(\lambda\{[\beta_2^2-\rho\beta_2\sqrt{(1-\beta_2^2)(1+\sigma^2)}]/E_{B2}\\ &\qquad +[1-\beta_2^2+\rho\beta_2\sqrt{(1-\beta_2^2)(1+\sigma^2)}]/E'_{B2}\\ &\qquad +(\gamma\sigma)^2[\beta_3^2/E_{B3}+(1-\beta_3^2)/E'_{B3}]\}\\ &\qquad +f_1f_2\lambda'\{[\rho^2(1-\beta_2^2)(1+\sigma^2)\\ &\qquad -\rho\beta_2\sqrt{(1-\beta_2^2)(1+\sigma^2)}]/E_{B2}\\ &\qquad +[\rho^2\beta_2^2(1+\sigma^2)+\rho\beta_2\sqrt{(1-\beta_2^2)(1+\sigma^2)}]/E'_{B2}\})\ , \end{aligned} \tag{8}$$

$$\begin{aligned}A_{11} &= \tfrac{1}{2}A-P\left[2.0023-g_{11}+\frac{4[1+(\lambda\sigma)^2]}{7[(1+\rho^2)(1+\sigma^2)+(\gamma\sigma)^2]}\right]+P'\left[\frac{4f_1^2\rho^2(1+\sigma^2)}{5[(1+\rho^2)(1+\sigma^2)+(\gamma\sigma)^2]}\right]\\ &\quad -\frac{1}{[(1+\rho^2)(1+\sigma^2)+(\gamma\sigma)^2]}\left\{\frac{3P}{7}\left[[1+(\gamma\sigma)^2]\left[\frac{\lambda}{w_1}\right]+\left[\frac{\lambda'}{w_2}\right]\right]\right.\\ &\qquad \left.-\frac{3P'}{5}\left[f_1\left[\frac{\lambda}{w_2}\right]+f_1^2\rho^2(1+\sigma^2)\left[\frac{\lambda'}{w_3}\right]\right]\right\}\ ,\end{aligned}$$

with

$$\begin{aligned}1/w_1 &\equiv \beta_2^2/E_{B2}+\beta_3^2/E_{B3}+(1-\beta_2^2)/E'_{B2}+(1-\beta_3^2)/E'_{B3}\ ,\\ 1/w_2 &\equiv f_1\rho\sqrt{1+\sigma^2}[f_2\beta_2\sqrt{1-\beta_2^2}(1/E'_{B2}-/E_{B2})+f_3\beta_3\sqrt{1-\beta_3^2}(1/E'_{B3}-1/E_{B3})]\ ,\end{aligned} \tag{9}$$

and

$$1/w_3 \equiv f_2^2(1-\beta_2^2)/E_{B2}+f_3^2(1-\beta_3^2)/E_{B3}+f_2^2\beta_2^2/E'_{B2}+f_3^2\beta_3^2/E'_{B3}\ .$$

$$\begin{aligned}A_{22} &= \tfrac{1}{2}A+\frac{2P}{7}\frac{[1+(\gamma\sigma)^2]}{[(1+\rho^2)(1+\sigma^2)+(\gamma\sigma)^2]}-\frac{2P'}{5}\frac{f_1^2\rho^2(1+\sigma^2)}{[(1+\rho^2)(1+\sigma^2)(\gamma\sigma)^2]}\\ &\quad -\frac{1}{[(1+\rho^2)(1+\sigma^2)+(\gamma\sigma)^2]}\left\{P\left[\frac{\lambda}{w_4}+\frac{\lambda}{w_5}+\frac{\lambda'}{w_6}\right]+P'\left[f_1\rho\sqrt{1+\sigma^2}\left[\frac{\lambda}{w_7}\right]+f_1^2\rho(1+\sigma^2)\left[\frac{\lambda'}{w_8}\right]\right]\right\}\ ,\end{aligned}$$

with

$$\begin{aligned}1/w_4 &\equiv 2\{\beta_2^2/E_{B2}+(1-\beta_2^2)/E'_{B2}+(\gamma\sigma)^2[\beta_3^2/E_{B3}+(1-\beta_3^2)/E'_{B3}]\}\\ &\qquad -\tfrac{3}{7}\{\beta_3^2/E_{B3}+(1-\beta_3^2)/E'_{B3}+(\gamma\sigma)^2[\beta_2^2E_{B2}+(1-\beta_2^2)/E'_{B2}]\}\ ,\\ 1/w_5 &\equiv (1/E'_{A1}-1/E_{A1})4\sqrt{3}\delta/[7(1+\delta^2)\sqrt{1+\gamma^2}]\ ,\\ 1/w_6 &\equiv f_1\rho\sqrt{1+\sigma^2}[2f_2\beta_2\sqrt{1-\beta_2^2}(1/E'_{B2}-1/E_{B2})+(3/7)f_3\beta_3\sqrt{1-\beta_3^2}(1/E_{B3}-1/E'_{B3})]\ ,\\ 1/w_7 &\equiv 2f_2\beta_2\sqrt{1-\beta_2^2}[(1/E'_{B2}-1/E_{B2})+\tfrac{3}{5}f_3\beta_3\sqrt{1-\beta_3^2}(1/E'_{B3}-1/E_{B3})]\ ,\end{aligned} \tag{10}$$

and

$$1/w_8 \equiv 2f_2^2[(1-\beta_2^2)/E_{B2}+\beta_2^2/E'_{B2}]+\tfrac{3}{5}f_3^2[(1-\beta_3^2)/E_{B3}+\beta_3^2/E'_{B3}] ,$$

where $g_{11} > g_{22} > g_{33}$ (which generally requires $E_{B2} < E_{B3}$), f_{A1} is the radial delocalization factor for states $|A_1\rangle$ and $|A'_1\rangle$, β_i and f_i belong to state $|B_i\rangle$, and g_{33}, A_{33} are given by expressions analogous to g_{22}, A_{22} but with subscripts 2 and 3 interchanged. λ and λ' are the spin-orbit coupling constants for copper $3d$ and $4p$ electrons, with values -828 and 925 cm^{-1}, respectively. P and P', given by $2.0023 g_N \mu_B \mu_N \langle r^{-3}\rangle$, are assigned their customary values of 0.036 and 0.040 cm^{-1} for the configurations $3d^9$ and $3d^{10}4p^{-1}$, respectively. The contact term is

$$\tfrac{1}{2}A=\{1/[(1+\rho^2)(1+\sigma^2)+(\gamma\sigma)^2]\}(-\kappa P[1+(\gamma\sigma)^2]+A_F^{4s}\{\sigma^2+[f_{A1}\lambda\gamma/(1+\delta^2)(1+\gamma^2)]^2(\delta^2/E_{A1}+E'_{A1})^2) . \tag{11}$$

Here $\kappa(0.43)$ is the isotropic contact interaction factor for the cupric ion, which reflects the net $|s\rangle$ hole density at the nucleus from core polarization, and A_F^{4s} is the Fermi coefficient of the $|4s\rangle$ orbital (0.2 cm^{-1}).

The simulations described earlier in the paper imply that the varied shapes and separations of the low-field quartet arise from inhomogeneous cupric sites which produce statistical variation in g_{11} and A_{11} correlated by $S=\Delta|A_{11}|/\Delta g_{11} \simeq -0.08$ cm^{-1}. Associated with the slight differences from the average structure are differences, e.g., $\delta\rho$, from the average values of the hybridization parameters. $\delta A_{11}/\delta g_{11}$ is readily formulated in terms of partial derivatives (calculated from the HAOM formulas) and the deviations of the hybridization parameters:

$$\frac{\delta A_{11}}{\delta g_{11}}=\frac{\dfrac{\partial A_{11}}{\partial\rho}\delta\rho+\dfrac{\partial A_{11}}{\partial\sigma}\delta\sigma+\dfrac{\partial A_{11}}{\partial\gamma}\delta\gamma}{\dfrac{\partial g_{11}}{\partial\rho}\delta\rho+\dfrac{\partial g_{11}}{\partial\sigma}\delta\sigma+\dfrac{\partial g_{11}}{\partial\gamma}\delta\gamma} . \tag{12}$$

Not present in Eq. (12) are contributions due to possible differences in the excited states associated with differences in structure. In this connection it should be noted that, because $|\lambda/E_{Bi}|<0.1$, g_{11} and A_{11} do not have significant contributions from the excited $|B_i\rangle$ states. A_{11} and g_{11} do depend upon states $|A_1\rangle$ and $|A'_1\rangle$ through $2.0023-g_{11}$. If the term $-P(2.0023-g_{11})$ were of importance in the correlation between A_{11} and g_{11}, then S would be close to the value of P; but this is clearly not the case because the value of P is $+0.0036$ cm^{-1} which differs in sign from $S(-0.08$ cm$^{-1})$. Changes in A_{11} and g_{11} associated with changes in $|A_1\rangle$ and $|A'_1\rangle$ may, to some extent, contribute to $\delta A_{11}/\delta g_{11}$, but this possibility is not included in Eq. (12) which reflects only properties of the ground state and generates an upper limit to S (i.e., a lower limit to $|S|$). Yet the values of S calculated with Eq. (12) tend to be more positive than -0.08 cm^{-1} (see Table II) rather than more negative (to offset a possible contribution from $|A\rangle$ and $|A'_1\rangle$, which would be positive). Thus the model-independent parameter S, obtained from analysis of the frequency dependence of the EPR spectra, is seen to impose a strong constraint upon the hybridization and delocalization parameters of the HAOM.

With ΔA_{11} linearly correlated with Δg_{11}, and both the numerator and denominator of Eq. (12) trilinear in $\delta\rho$, $\delta\sigma$, and $\delta\gamma$, these deviations are required to be in a fixed ratio. We assume then that, whatever atomic or charge disposition produces the average displacement of the cupric site symmetry away from planar (with resulting hybridization parameters ρ, σ, and γ), changes of this disposition from the average serve to increase or decrease the hybridization parameters proportionately, i.e.,

$$\delta\rho/\rho \simeq \delta\sigma/\sigma \simeq \delta\gamma/\gamma . \tag{13}$$

It follows that

$$\frac{\Delta A_{11}}{\Delta g_{11}}=\frac{\dfrac{\partial A_{11}}{\partial\rho}\rho+\dfrac{\partial A_{11}}{\partial\sigma}\sigma+\dfrac{\partial A_{11}}{\partial\gamma}\gamma}{\dfrac{\partial g_{11}}{\partial\rho}\rho+\dfrac{\partial g_{11}}{\partial\sigma}\sigma+\dfrac{\partial g_{11}}{\partial\gamma}\gamma} . \tag{14}$$

Optical measurements (absorption, circular dichroism, and magnetic circular dichroism) in the near-infrared and visible regions [3, 12–15] have established the existence of broad and overlapping transitions in azurin at 10 500, 13 000, 16 000, 18 500, 21 500, and 24 500 cm^{-1}. Absorption and circular dichroism measurements [14] suggest that there may also be a transition at about 7000 cm^{-1}. The band at 16 000 cm^{-1} could be the superposition of two bands only 100 cm^{-1} apart [3]. The manifold of states shown in Table I allows seven transitions from the ground state, and the corresponding energies appear in denominators of Eqs. (7)–(11). While there is no question that the strong transition at 16 000 cm^{-1} involves B_2 and/or B_3 states, because of the uncertainties in the 7000 and 16 000 cm^{-1} transitions mentioned above and the compatibility with the data of alternative ordering of several levels, several sets of assignments have been considered. In Table II representative cases are shown (orbital energies, hybridization coefficients, and radial delocalization factors) of the HAOM that generate magnetic parameters in agreement with those obtained from analysis of the experimental data.

The examples shown in Table II all have the centers of the states of Table I separated by 3000 cm^{-1}. We also investigated the effect that nearly degenerate states around 16 000 cm^{-1} would have on the magnetic parameters by setting the energies of the B_2 and B_3 states to be 16 500 and 15 500 cm^{-1}, respectively. With states this close in energy, the spin-orbit interaction that couples these states is a non-negligible fraction of the ligand field-induced energy splittings. Rigorous calculations of the magnetic properties therefore require that the nearly degenerate states be diagonalized with respect to the ligand field and spin-orbit interactions simultaneously in determining the actual composition of these nearby states. The details of this procedure, and its application to the calculation of magnetic circular dichroism parameters in low symmetry sites, are given in the Appendix of Ref. [19]. We carried out the analogous nearly degenerate treatment for the calculation of the g values in the present case and found that, with the $|B_2\rangle$ and $|B_2\rangle$ states separated by only 1000 cm^{-1}, the $g_{22}-g_{33}$ rhombicity is noticeably decreased. Without spin-orbit interaction coupling the $|B_2\rangle$ and $|B_3\rangle$ states, the $|B_2\rangle$ state is primarily responsible for $g_{33}-2.002\,3$ and the $|B_3\rangle$ state is primarily responsible for $g_{22}-2.002\,3$. With the inclusion of the spin-orbit coupling between these states, the final states are now each mixtures of both $|B_2\rangle$ and $|B_3\rangle$. This has the effect of decreasing any ligand-induced difference between the magnetic x and y axes and thus decreases the difference between g_{33} and g_{22} compared to a calculation that does not treat the states in a nearly degenerate fashion. Because the ligand field splitting is not expected to be zero (which would imply tetragonal symmetry) the final two states will not be equal combinations of $|B_2\rangle$ and $|B_3)$ and, therefore, some difference in g_{22} and g_{33} is still expected. We found though, that to get a calculated rhombicity ($g_{22}-g_{33}$) of approximately 0.017, as observed experimentally, the hybridization parameters β_2 and β_3 have to differ from one another, e.g., 0.75 and 1.00, respectively, noticeably more than for the cases listed in Table II. But there is an inconsistency in β_2 and β_3 being very different while the ligand field splitting of states $|B_2\rangle$ and $|B_3\rangle$ is small; for the states to be only 1000 cm^{-1} apart implies that the ligand field makes only a small distinction between the two states and therefore the hybridization coefficients of the states, β_2 and β_3, should also be similar. Therefore we believe that the experimentally observed rhombicity in g values requires that $|B_2\rangle$ and $|B_3\rangle$ be further apart than 1000 cm^{-1}. However, the differences in the values of β_2 and β_3 for the cases in Table II are physically consistent with the energy difference of 3000 cm^{-1} between the $|B_2\rangle$ and $|B_3\rangle$ states.

The ranges of ρ, σ, and $|\gamma|$ for which agreement is found between measured parameters and those calculated with the HAOM model are surprisingly narrow. ρ is in the range 0.65–0.72, σ in the range 0.22–0.26, and $|\gamma|$ in the range 0.44–0.58. It follows that the solid angle within which the direction of maximum concentration of ground-state orbital is to be found is small. This direction, obtained from calculus in the usual way, is given by

$$\cos\theta_{\mathrm{max.ampl.}}=\pm\rho\sqrt{(1+\sigma^2)}/\sqrt{5(1+\gamma^2\sigma^2)}\ , \tag{15}$$

and

$$\cot(2\phi)_{\mathrm{max.ampl.}}=-\gamma\sigma\ . \tag{16}$$

where θ and ϕ are the spherical coordinates appropriate to the x,y,z, system of Table I. With $\rho=0.70,\sigma=0.23$, and $\gamma=0.50,\theta_{\mathrm{max.ampl.}}=71.4°$ (or 18.6° out-of-plane) and $\phi_{\mathrm{max.ampl.}}=-41.9°$. The ground-state hole density is seen to be tetrahedrally distorted away from the planar concentration of the lobes of the $3d_{xy}$ orbital (and also slight-

TABLE II. Magnetic parameters generated by hybrid-atomic-orbital models for the single cupric hole in azurin.

Energies ($\mathrm{k\,cm}^{-1}$)							Hybridization parameters						Radial delocalization				Spin-Hamiltonian parameters						Correl.
A_1	A_1'	B_2	B_3	B_1'	B_2'	B_3'	ρ	β_2	β_3	γ	σ	δ	f_{A1}	f_{B1}	f_{B2}	f_{B3}	g_{11}	g_{22}	g_{33}	A_{11}[a]	A_{11}[a]	A_{22}[a]	S
7.0	10.0	16.0	13.0	19.0	22.0	25.0	0.69	0.85	0.92	0.58	0.23	−0.75	0.73	1.00	1.00	1.00	2.269	2.053	2.036	54	−12	−15	−0.079
							0.70	0.88	0.93	0.60		−0.17	0.85								−13	−18	−0.076
							0.76		0.95	0.53	0.25	−0.23		0.85	0.85	0.85					13	8	−0.069
										0.54		−0.93	0.73								12	10	−0.067
10.0	7.0						0.70		0.93	0.78	0.23	4.00	1.00	1.00	1.00	1.00					−14	−18	−0.056
										0.60		6.00	0.85								−13	−18	−0.076
												1.18	0.73								−14	−17	
							0.73	0.91	0.95			0.99		0.95	0.95	0.95					−11	−13	−0.068
							0.80	0.95	0.98			1.59	0.85	0.85	0.85	0.85					3	−5	−0.056
							0.81	0.96	0.99			0.60	0.73								−4	−7	−0.055

[a] In units of $10^{-4}\ \mathrm{cm}^{-1}$.

ly rhombic). A single-crystal EPR orientation study of cupric azurin remains to be carried out, and so the orientation of the spectroscopic principal directions with respect to the crystal axes is not yet known. The single-crystal measurements are clearly of great importance; the results will enable one to relate the electron density function of the ground state arrived at from spectroscopic measurements to the three-dimensional structure around the cupric ion available from x-ray diffraction.

STRUCTURAL DISTRIBUTIONS AND FORCE CONSTANTS

Associated with a distribution in structure are distributions in hybridization parameters. Thus, for the ground state, there will be spreads σ_ρ, σ_σ, and σ_γ in the parameters ρ, σ, and γ. These spreads will be taken in the ratio $\sigma_\rho:\sigma_\sigma:\sigma_\gamma=\rho:\sigma:\gamma$ as were their deviations, Eq. (13). It follows that

$$\sigma_g=\sigma_{g_{11}}=\frac{\partial g_{11}}{\partial\rho}\sigma_\rho+\frac{\partial g_{11}}{\partial\sigma}\sigma_\sigma+\frac{\partial g_{11}}{\partial\gamma}\sigma_\gamma\ . \tag{18}$$

For $\rho=0.70, \sigma=0.23$, and $\gamma=0.50$, the partial derivatives are

$$\frac{\partial g_{11}}{\partial\rho}=-0.245,\quad \frac{\partial g_{11}}{\partial\sigma}=-0.120,\quad \frac{\partial g_{11}}{\partial\gamma}=-0.226\ . \tag{19}$$

With the value $\sigma_g=0.009$ arrived at from matching simulated to measured spectra, one obtains

$$\sigma_\rho=0.020,\quad \sigma_\sigma=0.0066,\quad \sigma_\gamma=0.014\ . \tag{20}$$

Equations (15) and (16) then provide spreads in the angles $\theta_{\text{max.ampl.}}$ and $\phi_{\text{max.ampl.}}$ of $\sigma_\theta=0.6°(0.01\text{ rad})$ and $\sigma_\phi=0.2°(0.0035\text{ rad})$, respectively.

If the structural changes responsible for the spreads in the hybridization parameters result from normal modes frozen in at about 200 K, then equipartition can be employed to obtain force constants. Changes in θ are then seen to arise from a tetrahedral bending mode affecting the tetrahedrally disposed four lobes of the distorted $3d_{xy}$ ground orbital. Corresponding to the spread σ_θ there are four linear displacements of 0.02 Å for copper-ligand bond lengths of 2 Å. The force constant calculated on this basis is 1.7×10^5 dyn/cm, large for a bending mode but understandable in terms of the constraining influence of the protein in determining the geometry of the metal site. From the spread in ϕ, σ_ϕ, a force constant of 14×10^5 dyn/cm is obtained, about an order of magnitude stiffer than from θ and in the range for stretch modes. Thus the combination of copper and protein force components that constrain the ϕ rotation of the orbitals do so significantly more rigidly than do those that constrain the θ motion. In the HAOM quantified here, the stiffness of ϕ displacement is related to the small amount of $3d_{x^2-y^2}$ mixed into the ground state.

DISCUSSION

Quantitative information about force constants, obtained from the analysis given here, is necessary for understanding the mechanics of proteins and, in conjunction with resonance Raman data [36], of potential use in characterizing normal modes. Further, the force constants enter treatment of thermal activation of electron transfer processes [37], and the resulting formulation can be applied to the blue cupric proteins [38].

Interpretation of the spreads in hybridization parameters in terms of force constants and equipartition is based upon the freezing in of vibrational modes [7]. Do the spreads in site geometry arise mainly from freezing in vibrational modes, or is freezing-induced structural strain more important? Information from this laboratory indicates that stresses associated with formation of ice crystallites are not a major factor in producing the structural inhomogeneities found in high-spin ferric myoglobins and hemoglobins at low temperatures. For example, the aquo, methanol, and ethanol complexes of these proteins (frozen under the same conditions and with the alcohols at concentrations too low to affect the freezing process) have different and characteristic spreads in E/D (ratio of rhombic to tetragonal strengths of the ligand field) and $\eta_{\text{s.o.}}$ (spin-orbit depletion of the ground sextuplet) [39]. Conversely, the value of σ_1 (rms spread in energy of the first excited electronic level of heme iron) is the same for frozen crystals as for solutions of aquo ferric myoglobin, wherein the size distributions of ice crystallites almost certainly differ [9]. With regard to azurin itself, addition of glycerol (believed to reduce the size of ice crystallites and promote glass formation) has little effect upon the EPR spectrum [22]. The information presented in the preceding sentences also argues against random electric-field contributions from inhomogeneously frozen solvent (water) as a major source of distributions in hybridization parameters; it should be noted that the copper is shielded from the solvent by a hydrophobic surface region [10], an environment which keeps the polar solvent away from the metal ion and reduces interactions between the two.

Thus the data at hand indicate that, at least for the proteins just discussed, structural inhomogeneities revealed by EPR spectroscopy at low temperatures are primarily characteristic of the macromolecules, with properties of the ice phase around them playing a secondary role. The extent of this secondary role should be evaluated because, as discussed above, quantitative information about force constants is needed. Fortunately, a means for investigating and controlling stress-producing conditions associated with freezing is now available [40]. [Stress is caused by the growth of ice crystallites and the expulsion of solutes from ice as it is formed, resulting in regions of concentrated solute. The extreme conditions are (1) homogeneous solute distribution and small ice crystallites, achieved by very rapid freezing of a solution rich in, for example, sucrose; (2) inhomogeneous solute distribution and large ice crystallites, achieved by very slow freezing of a solution with minimal solutes.] The distributions in g and A tensors associated with protein modes could be joined by a contribution from iceproduced strain, the magnitude of the latter depending upon the conditions of freezing.

The structural model-based treatment of distributed spin-Hamiltonian parameters given above depends upon considerable knowledge of the paramagnetic center, such that a substantial number of electronic levels can be employed with some confidence. When this is not the case, model-independent analysis is required, examples of which can be found in the first part of this paper and elsewhere [41].

CONCLUSION

EPR spectra at *J*-, *X*-, and *Ka*-band frequencies from azurin in frozen solution at 77 K reflect correlated distributions in the leading principle values of the g and A tensors. Simulations based upon a linear relation between A_{11} and g_{11} reproduce salient features of the experimental spectra, provide accurate principal values of the g and A tensors, and quantify the rms deviation of the distribution in g_{11} and the correlation factor $S=\Delta|A_{11}|/\Delta g_{11}$. All of these experimentally obtained, model-independent parameters, are readily generated with formulas derived from a hybrid atomic orbital model when the energies of the excited states are taken from band analysis of optical spectra (absorptivity, circular dichroism, and magnetic circular dichroism). Sets of hybridization parameters which produce magnetic (and optical) properties consistent with experimental data generate ground-state orbitals which are closely related in their low-symmetry components. Possible sources for the mixing of excited levels of the free cupric ion into the predominantly $3d_{xy}$ ground state of the bound metal are apparent. The four closest atoms, two nitrogens and two sulfurs, are constrained by the protein to a configuration of low symmetry. An electric field of low symmetry due to charges on amino acid side chains will be present. It should also be noted that the electric dipole polarizability of sulfur is about three times greater than that of nitrogen.

The distribution in geometry of the ground-state orbital was quantitatively interpreted above in terms of modes of motion, and equipartition yielded sensible force constants. There can also be a contribution to the spread in hybridization parameters from a distribution in electric field at the cupric site. Whatever the source, analysis of the experimental spectra shows that the ground state of the cupric ion in azurin differs significantly from molecule to molecule. There are no compositional or covalent differences among these protein molecules. Clearly then, at the temperature of the living system, cupric sites in azurin are undergoing fluctuations in electronic structure of the kind described above and of greater amplitude. Among such fluctuations are ones which bring the structure closer to that preferred by the cuprous ion, thereby increasing the probability of electron transfer to the cupric site when an electron donor is present. The effect of such structural fluctuations upon thermal activation of tunneling has been treated quantitatively [37].

ACKNOWLEDGMENTS

The klystron used as a microwave source at 6 GHz was kindly loaned by Professor Charles M. Grisham. We thank Professor Joseph J. Villafranca for sharing with us his design of a variable temperature dewar for use with the 35-GHz cavity. The possibility that the metal binding site in azurin is subject to conformational fluctuations that are frozen in when the sample is cooled, resulting in a fixed distribution in g_{11} and A_{11} values, was originally suggested by Dr. Nicholas J. Hill. Support from the National Science Foundation under Grant Nos. PCM-7904361, PCM-8104377, and DMB-8517819 is acknowledged with appreciation. Partial financial support was also provided by a Biomedical Research Support Grant from the National Institutes of Health, and we are appreciative of this assistance.

---

*Present address: Department of Radiology, School of Medicine, University of Virginia, Charlottesville, VA 22908.

[1] J. H. Van Vleck, *Electric and Magnetic Susceptibilities* (Oxford, London, 1932).

[2] A. S. Brill, *Transition Metals in Biochemistry* (Springer, Berlin, 1977).

[3] A. Aqualino, Ph.D. thesis, University of Virginia, 1982.

[4] A. S. Brill, F. G. Fiamingo, and D. H. Hampton, in *Frontiers of Biological Energetics,* edited by P. L. Dutton *et al.* (Academic, New York, 1978), Vol. 2, p. 1025.

[5] C. E. Schulz, R. Rutter, J. T. Sage, P. G. Debrunner, and L. P. Hager, Biochem. **23**, 4743 (1984).

[6] P. M. Champion and A. J. Sievers, J. Chem. Phys. **72**, 1569 (1980).

[7] A. S. Brill, in *Tunneling in Biological Systems,* edited by B. Chance *et al.* (Academic, New York, 1979), p. 561.

[8] P. G. Debrunner and H. Frauenfelder, Annu. Rev. Phys. Chem. **33**, 283 (1982).

[9] A. S. Brill, F. G. Fiamingo, D. A. Hampton, P. D. Levin, and R. Thorkildsen, Phys. Rev. Lett. **54**, 1864 (1985); P. Levin and A. S. Brill, J. Phys. Chem. **92**, 5103 (1988); F. G. Fiamingo, A. S. Brill, D. A. Hampton, and R. Thorkildsen, Biophys. J. **55**, 67 (1989).

[10] E. T. Adman and L. H. Jensen, Isr. J. Chem. **21**, 8 (1981).

[11] G. E. Norris, B. F. Anderson, and E. N. Baker, J. Mol. Biol. **165**, 501 (1983).

[12] A. S. Brill, G. F. Bryce, and H. J. Maria, Biochem. Biophys. Acta **154**, 342 (1968).

[13] S. -P. W. Tang, J. E. Coleman, and Y. P. Meyer, J. Bio. Chem. **243**, 4286 (1968).

[14] E. I. Solomon, J. W. Hare, D. M. Dooley, J. H. Dawson, P. J. Stephens, and H. B. Gray, J. Am. Chem. Soc. **102**, 168 (1980).

[15] C. Greenwood, B. C. Hill, D. Barber, D. G. Eglinton, and D. J. Thomson, Biochem. J. **215**, 303 (1983).

[16] G. H. Rist, J. S. Hyde, and T. Vänngård, Proc. Nat. Acad. Sci. **67**, 79 (1970).

[17] C. A. Bates, W. S. Moore, K. H. Standley, and K. W. H. Stevens, Proc. Phys. Soc. **79**, 73 (1962); C. A. Bates, *ibid.* **83**, 465 (1964).

[18] A. S. Brill and G. F. Bryce, J. Chem. Phys. **48**, 4398

(1968).

[19] B. S. Gerstman and A. S. Brill, J. Chem. Phys. **82**, 1212 (1985).

[20] B. S. Gerstman and A. S. Brill, Phys. Rev. A **37**, 2151 (1988); **39**, 5903 (1989).

[21] W. Froncisz and J. S. Hyde, J. Chem. Phys. **73**, 3123 (1980).

[22] C. M. Groeneveld, R. Aasa, B. Reinhammar, and G. W. Canters, J. Inorg. Biochem. **31**, 143 (1987).

[23] N. J. Hill (unpublished experiments).

[24] Simulations of EPR spectra reported in this paper are based upon a program developed by J. H. Venable, Jr., and described in his Ph. D. thesis, Yale University, 1965.

[25] G. E. Pake and T. L. Estle, in *The Physical Principles of Electron Paramagnetic Resonance,* 2nd ed. (Benjamin, Reading, MA, 1973), Appendix B, p. 298.

[26] J. G. M. Van Rens, C. P. Keijzers, and H. Van Willigen, J. Chem. Phys. **52**, 2858 (1970).

[27] W. B. Lewis, M. Alei, and L. O. Morgan, J. Chem. Phys. **44**, 2409 (1966).

[28] D. Kivelson and R. Neiman, J. Chem. Phys. **35**, 149 (1961).

[29] A. M. Mood, F. A. Graybill, and D. C. Boes, in *Introduction to the Theory of Statistics* (McGraw-Hill, New York, 1974), p. 162.

[30] T. Vänngård, in *Biological Applications of Electron Spin Resonance,* edited by H. Schwartz *et al.* (Wiley, New York, 1972), p. 411.

[31] C. Mailer and C. P. S. Taylor, Can. J. Biochem. **49**, 695 (1971).

[32] A. S. Brill, R. B. Martin, and R. J. P. Williams, in *Electronic Aspects of Biochemistry,* edited by B. Pullman (Academic, New York, 1964), p. 519.

[33] K. W. H. Stevens, Proc. R. Soc. London Ser. A **219**, 542 (1953).

[34] K. W. Penfield, A. A. Gewirth, and E. I. Solomon, J. Am. Chem. Soc. **107**, 4519 (1985).

[35] A. Abragam and M. H. L. Pryce, Proc. R. Soc. London Ser. A **205**, 135 (1951).

[36] M. Belhadj, J. M. Jean, R. A. Friesner, J. Schoonover, and W. H. Woodruff, J. Phys. Chem. **94**, 2160 (1990).

[37] J. J. Hopfield, Proc. Nat. Acad. Sci. **71**, 3640 (1974).

[38] A. S. Brill, Biophys. J. **22**, 139 (1978).

[39] A. S. Brill, F. G. Fiamingo, and D. A. Hampton, J. Inorg. Biochem. **28**, 137 (1986).

[40] A. -S. Yang and A. S. Brill, Biophys. J. **59**, 1050 (1991).

[41] W. R. Hagen, D. O. Hearshen, R. H. Sands, and W. R. Dunham, J. Mag. Res. **61**, 220 (1985).